HAL
open science

Coulombic self-ordering upon charging a large-capacity layered cathode material for rechargeable batteries

Benoit Mortemard de Boisse, Marine Reynaud, Jiangtao Ma, Jun Kikkawa, Shin-Ichi Nishimura, Montse Casas-Cabanas, Claude Delmas, Masashi Okubo, Atsuo Yamada

To cite this version:

Benoit Mortemard de Boisse, Marine Reynaud, Jiangtao Ma, Jun Kikkawa, Shin-Ichi Nishimura, et al.. Coulombic self-ordering upon charging a large-capacity layered cathode material for rechargeable batteries. Nature Communications, 2019, 10, 2185 (7 p.). 10.1038/s41467-019-09409-1 . hal-02135401

HAL Id: hal-02135401

https://hal.science/hal-02135401

Submitted on 16 Jul 2020

HAL is a multi-disciplinary open access archive for the deposit and dissemination of scientific research documents, whether they are published or not. The documents may come from teaching and research institutions in France or abroad, or from public or private research centers.

L'archive ouverte pluridisciplinaire **HAL**, est destinée au dépôt et à la diffusion de documents scientifiques de niveau recherche, publiés ou non, émanant des établissements d'enseignement et de recherche français ou étrangers, des laboratoires publics ou privés.

nature COMMUNICATIONS

ARTICLE

https://doi.org/10.1038/s41467-019-09409-1 OPEN

Coulombic self-ordering upon charging a large-capacity layered cathode material for rechargeable batteries

Benoit Mortemard de Boisse[1], Marine Reynaud[2], Jiangtao Ma[1], Jun Kikkawa[3], Shin-ichi Nishimura[1,4], Montse Casas-Cabanas[2], Claude Delmas[5], Masashi Okubo[1,4] & Atsuo Yamada[1,4]

Lithium- and sodium-rich layered transition-metal oxides have recently been attracting significant interest because of their large capacity achieved by additional oxygen-redox reactions. However, layered transition-metal oxides exhibit structural degradation such as cation migration, layer exfoliation or cracks upon deep charge, which is a major obstacle to achieve higher energy-density batteries. Here we demonstrate a self-repairing phenomenon of stacking faults upon desodiation from an oxygen-redox layered oxide Na_2RuO_3, realizing much better reversibility of the electrode reaction. The phase transformations upon charging A_2MO_3 (A: alkali metal) can be dominated by three-dimensional Coulombic attractive interactions driven by the existence of ordered alkali-metal vacancies, leading to counter-intuitive self-repairing of stacking faults and progressive ordering upon charging. The cooperatively ordered vacancy in lithium-/sodium-rich layered transition-metal oxides is shown to play an essential role, not only in generating the electro-active nonbonding 2*p* orbital of neighbouring oxygen but also in stabilizing the phase transformation for highly reversible oxygen-redox reactions.

[1] Department of Chemical System Engineering, School of Engineering, The University of Tokyo, Hongo 7-3-1, Bunkyo-ku, Tokyo 113-8656, Japan. [2] CIC energiGUNE, Parque Tecnológico de Álava, 01510 Vitoria-Gasteiz, Álava, Spain. [3] Advanced Key Technologies Division, National Institute for Materials Science, Tsukuba, Ibaraki 305-0044, Japan. [4] Elements Strategy Initiative for Catalysts & Batteries (ESICB), Kyoto University, Nishikyo-ku, Kyoto 614-8245, Japan. [5] Institut de Chimie de la Matière Condensée de Bordeaux (ICMCB), 33600 Pessac, France. Correspondence and requests for materials should be addressed to A.Y. (email: yamada@chemsys.t.u-tokyo.ac.jp)

The discovery of intercalation chemistry in layered transition-metal oxides AMO_2 (A=Li, Na and M=transition metal)[1,2] in the early 1980s has led to the commercialization of lithium-ion batteries[3]. Tremendous effort has since been devoted to understanding how alkali-metal ions reversibly (de)intercalate in AMO_2 because this is essential to exploit their large theoretical capacities (~275 mAh g^{-1} for $LiCoO_2$ and ~235 mAh g^{-1} for $NaCoO_2$, respectively). It is now well understood that, at the early stage of A^+ deintercalation, A_xMO_2 ($0.4 < x < 1.0$) exhibit an increase of their interlayer distance because the depletion of screening A^+ layers enhances the effective Coulombic repulsion between oxide ions of adjacent MO_2 layers[4–8]. At the late stage of A^+ deintercalation ($0.0 < x < 0.4$), high-valent M increases the covalency of M−O bonds, and thus decreases the negative charge on oxide ions. In this situation, O−O van der Waals attraction forces are not sufficient to maintain the layered structure, and the large volume variations induced at the end of charge often initiate crack formation and delamination/exfoliation[8–10]. Furthermore, the lack of alkali ions in the interlayer space leads to structural degradation with migration of transition-metal ions to neighboring tetrahedral sites[11–13]. This established knowledge on the intercalation chemistry of A_xMO_2 explains the practical limit of their reversible capacity (approximately for $0.4 < x < 1.0$, i.e., 170 mAh g^{-1} for A = Li and 140 mAh g^{-1} for A = Na). Therefore, the control of the competing Coulombic and van der Waals forces in layered transition-metal oxides is of great importance to achieve a large reversible capacity.

Layered *A*-excess transition-metal oxides ($A_{1+y}M_{1-y}O_2$ or $A_1[A_yM_{1-y}]O_2$) are recent major targets to increase the cathode capacity by virtue of additional oxygen-redox reactions. Li_2MnO_3-$LiMO_2$ solid solutions have been reported to deliver large capacities over 200 mAh g^{-1}[14–16], and have more recently been followed by Li_2MO_3 (M = Ru[17], Ir[18], RuSn[17], and RuMn[19]) and Na_2MO_3 (M = Ru[20,21], RuSn[21], and Ir[22]), all delivering large capacities exceeding that of solely M redox. Although the changes in the electronic state during the additional oxygen-redox reactions have been intensively investigated, less attention has been paid to the essential interaction dominating the phase transformation during the charge/discharge processes, presumably because most oxygen-redox electrodes exhibit severe structural degradation (i.e., oxygen-gas evolution, cation migration) at the initial charge[16,17,23,24]. However, the extra A^+ are expected to play a crucial role in the structural transformation during the charge/discharge processes. For example, the depletion of screening A^+ layers upon charging can be compensated by the A^+ supplied from the $[A_yM_{1-y}]O_2$ layers[18,20,22]. Moreover, A^+ (or vacancy after deintercalation) in the $[A_yM_{1-y}]O_2$ layers is expected to modulate the balance of competing Coulombic/van der Waals forces, and hence largely influence the intercalation chemistry.

We have recently studied the structure and electrochemistry of O3-Na_2RuO_3 (or $Na[Na_{1/3}Ru_{2/3}]O_2$), where $[Na_{1/3}Ru_{2/3}]O_2$ layers have a honeycomb-type ordered arrangement of Na and Ru[20,25]. According to the classification of layered oxides, O3 denotes a structure where Na^+ ions occupy octahedral interlayer sites and

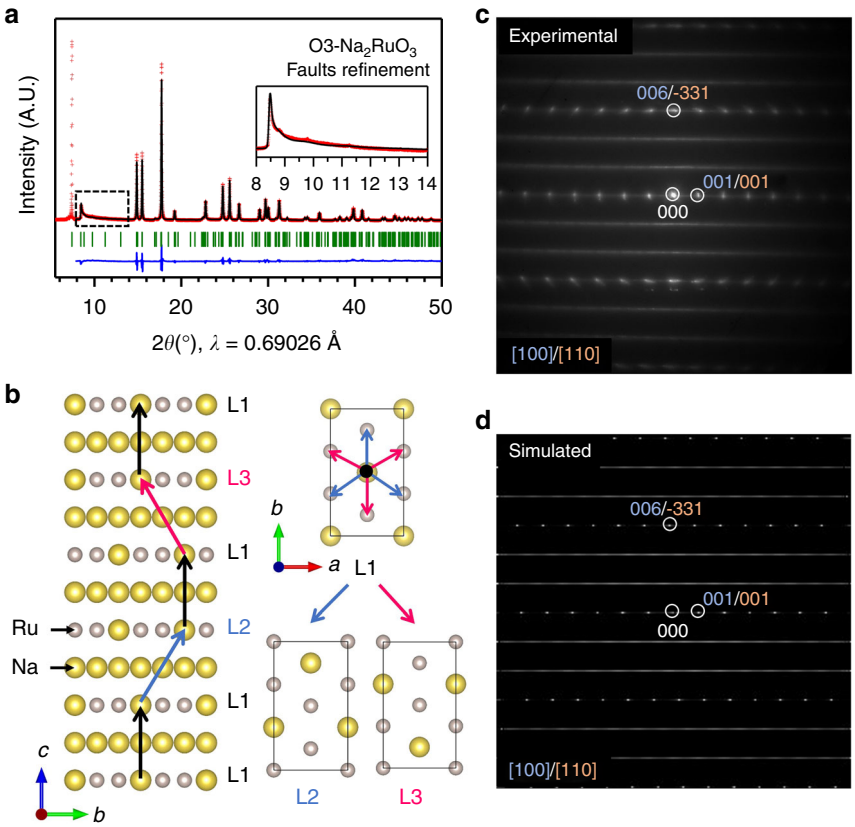

Fig. 1 Stacking faults in Na_2RuO_3. **a** Observed and calculated (FAULTS refinement) synchrotron XRD patterns of O3-Na_2RuO_3 (pristine state). Observed data, the calculated pattern, and the difference between observed and calculated data are shown as plus sign (red), solid line (black) and continuous line (blue), respectively. The positions of Bragg reflections are indicated by vertical tick marks (green). The first diffraction peak has been excluded from the refinement due to important asymmetry that FAULTS does not take into account. The insert is a zoom of the initial superstructure peaks (Warren fall). **b** Representation of the stacking faults in O3-Na_2RuO_3, using the FAULTS unit cell described in the text. **c**, **d** Experimental and simulated SAED pattern along the [100] (= <$[110]_{C2/m}$>) direction, respectively

the stacking of oxide ions is ABCABC (Supplementary Fig. 1)[26]. Importantly, in contrast to most oxygen-redox electrodes, O3-Na_2RuO_3 exhibits highly reversible (de)sodiation without structural degradation but rather exhibits progressive structural ordering upon charging, which provides an opportunity for not only detailed structural investigation as a model system but also for essential strategies toward much larger reversible capacity.

In this work, synchrotron X-ray diffraction coupled with planar-defect refinement analyses are applied to honeycomb ordered Na_xRuO_3 phases ($x = 2$, 1, and 1/2), revealing a self-repairing phenomenon of stacking faults upon charging, which significantly stabilizes the reversible large capacity operation. Driving force of the 3D self-ordering is strong long-range cooperative Coulombic interactions between MO_3 slabs intermediated by ordered vacancies.

Results

Stacking faults in Na_2RuO_3. O3-Na_2RuO_3 was synthesized by decomposing Na_2RuO_4 at 850 °C for 12 h under Ar atmosphere[20,25]. Figure 1a shows the experimental and calculated synchrotron XRD patterns of O3-Na_2RuO_3, in which the most of intense diffraction peaks can be fitted by the usual rhombohedral lattice of O3-AMO_2 layered oxides[20]. However, the main difficulty hindering an accurate pattern fit lies in the broad nature of some diffraction peaks and diffuse scatterings, which are highlighted by the dashed rectangle in Fig. 1a. Such broadening is typically observed for A_2MO_3 with honeycomb ordered $[A_{1/3}M_{2/3}]O_2$ layers, and arises from stacking disorder. These stacking faults can be described by an occasional shift of the $[A_{1/3}M_{2/3}]O_2$ layers perpendicularly to the stacking direction. In fact, in layered materials, the crystal grows perpendicularly to the layer plane. When a nucleation starts in a wrong position, a stacking fault appears while the oxygen packing remains ideal. As a result, the honeycomb ordering of the $[A_{1/3}M_{2/3}]O_2$ layers is maintained but the honeycomb stacking deviates from the ideal sequence (Fig. 1b), which causes the peculiar asymmetric peak broadening (Warren fall) observed in Fig. 1a as well as the diffuse streaks on the selected area electron diffraction (SAED) pattern along the $[100]-\langle 110\rangle_{C2/m}$ direction (Fig. 1c).

To refine the powder diffraction data for the structure containing stacking faults, a FAULTS analysis, which allows the incorporation of the occurrence probabilities of possible stackings, was conducted[27]. As shown in Fig. 1a (Supplementary Tables 1 and 2), the FAULTS analysis provides a satisfactory

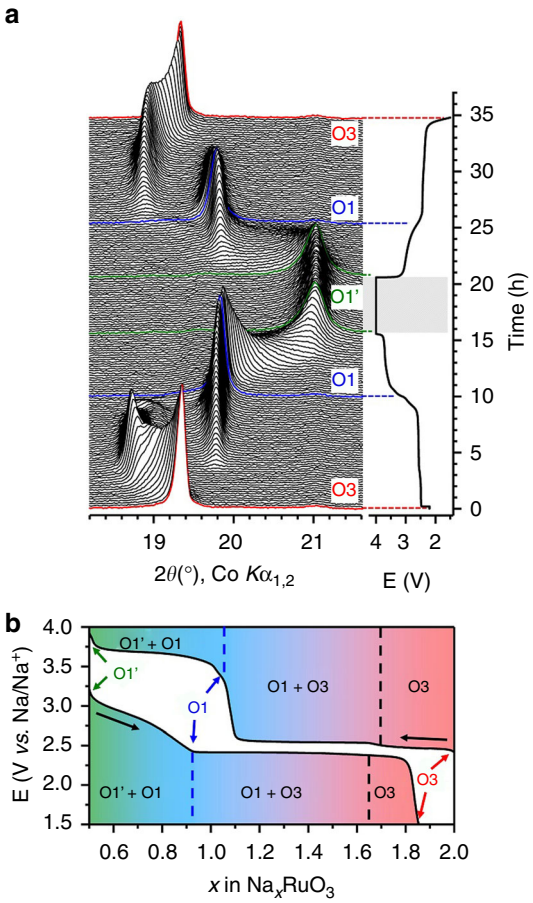

Fig. 2 Structural evolution upon charging/discharging Na_2RuO_3. **a** XRD patterns recorded in situ during the first cycle of Na_2RuO_3 with the corresponding cycling curve. The dashed area corresponds to a potentiostatic break whose aim was to ensure the equilibrium state at 4.0 V before discharging the cell. **b** Phase diagram as determined from the in situ experiment as a function of the sodium content

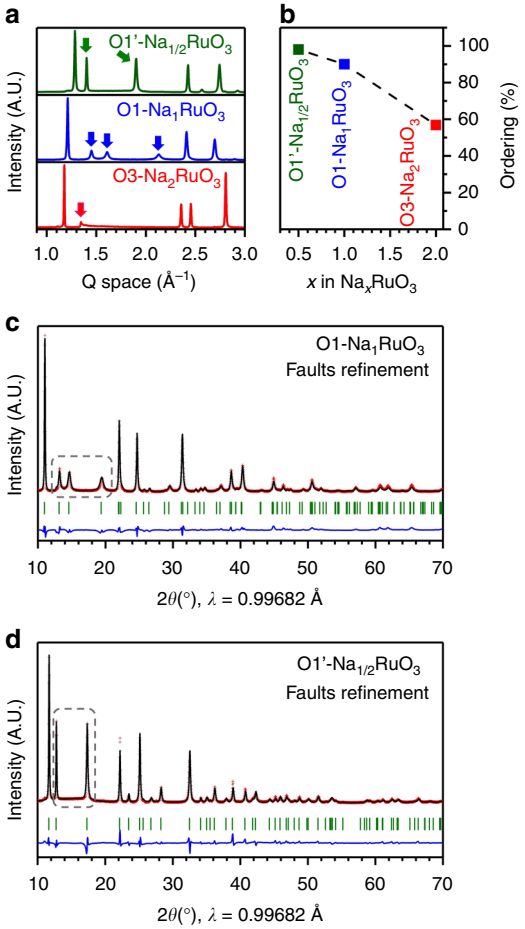

Fig. 3 Progressive stacking-fault-depression (self-ordering) upon charging Na_2RuO_3. **a** Synchrotron XRD patterns of O3-Na_2RuO_3, O1-Na_1RuO_3 and O1′-$Na_{1/2}RuO_3$. Arrows indicate the most intense superstructure peaks. **b** Evolution of the ordered stacking (absence of stacking faults) as a function of the Na content. The error bars are smaller than the mark size. **c**, **d** Observed and calculated (FAULTS refinement) synchrotron XRD patterns of O1-Na_1RuO_3 and O1′-$Na_{1/2}RuO_3$, respectively. Red crosses: experimental, black line: calculated, blue line: difference plot and green bars: Bragg positions in the $R\bar{3}$:h and $P\bar{3}1m$ space groups for O1-Na_1RuO_3 and O1′-$Na_{1/2}RuO_3$, respectively. The dashed rectangles indicate the most intense superstructure peaks

description of the superstructure peaks and indicates the occurrence of ~40% stacking faults between the $[Na_{1/3}Ru_{2/3}]O_2$ layers in pristine O3-Na_2RuO_3. This result is further supported by the FAULTS-simulated SAED pattern that well reproduces the diffuse streaks observed in the experimental SAED pattern (Fig. 1d).

After evaluation of the stacking faults in pristine O3-Na_2RuO_3, we studied the structural evolution of Na_xRuO_3 during the first charge and discharge using in situ XRD. Figure 2 shows that the phase transformation of Na_xRuO_3 involves three main phases: O3-Na_xRuO_3, O1-Na_1RuO_3, and O1′-$Na_{1/2}RuO_3$. (De)sodiation at 2.7 V vs. Na/Na^+ ($1.0<x<2.0$) mainly proceeds through a two-phase process between O3-Na_xRuO_3 and O1-Na_1RuO_3. As reported previously, O1-Na_1RuO_3 has an ilmenite-type structure (ABAB oxide-ions stacking and Na^+ ions in interlayer octahedral sites) where the honeycomb ordered $[Ru_{2/3}\square_{1/3}]O_2$ and $[Na_{2/3}\square_{1/3}]O_2$ layers (□: Na^+ vacancy) stack alternatively (Supplementary Fig. 2)[20]. At the second charging plateau, a new phase (O1′-$Na_{1/2}RuO_3$) with a shorter interlayer distance (4.91 Å vs. 5.21 Å for O1-Na_1RuO_3) appears at the expense of the O1 phase. Its structure was determined from the synchrotron XRD pattern of an electrochemically deintercalated sample, whose Rietveld refinement is presented in Supplementary Fig. 3 and Supplementary Table 3. The diffraction peaks are successfully indexed in a hexagonal lattice with $P\bar{3}1m$ symmetry with $a = 5.1876(9)$ Å and $c = 4.906(1)$ Å. As the oxide-ion stacking sequence is ABAB and Na^+ occupies an octahedral site, we will refer to this phase as O1′-$Na_{1/2}RuO_3$, where the alternate stacking of the honeycomb ordered $[Ru_{2/3}\square_{1/3}]O_2$ and $[Na_{1/3}\square_{2/3}]O_2$ layers is maintained. Then, the difference between the O1 and O1′ structures lies in the Na content and on the respective stacking of the $[Ru_{2/3}\square_{1/3}]O_2$ layers, which are shifted from one another in O1-Na_1RuO_3 while directly stacked in O1′-$Na_{1/2}RuO_3$ (Supplementary Figs. 2 and 3). It is noteworthy that the superstructure peaks highlighted by the arrows in Fig. 3a exhibit remarkable sharpening upon charging. This suggests that stacking faults tend to disappear, assisted by the adjustable layer gliding involved in the O3→O1′ transition. The FAULTS refinements (Fig. 3c, d and Supplementary Tables 4–6) indicate that the occurrence probability of stacking faults indeed decreases from 40% in O3-Na_2RuO_3 to 10% (O1-Na_1RuO_3) and then to 2% (O1′-$Na_{1/2}RuO_3$) (Fig. 3b). Therefore, Na^+ deintercalation (charging) from Na_2RuO_3 involves a self-reorganization process that significantly diminishes the initial amount of stacking faults. Importantly, the stacking faults are reformed after discharging, making this ordering/faulting process reversible, even after several cycles (Supplementary Figs. 4 and 5).

Self-ordering of stacking faults upon charging Na_2RuO_3. Based on the complete knowledge of the structural evolution from O3-Na_2RuO_3 to O1-Na_1RuO_3, and then to O1′-$Na_{1/2}RuO_3$, let us now consider the Coulombic origin of the consolidation on the phase transformation with the effect of gliding vectors $\vec{t}$ of the

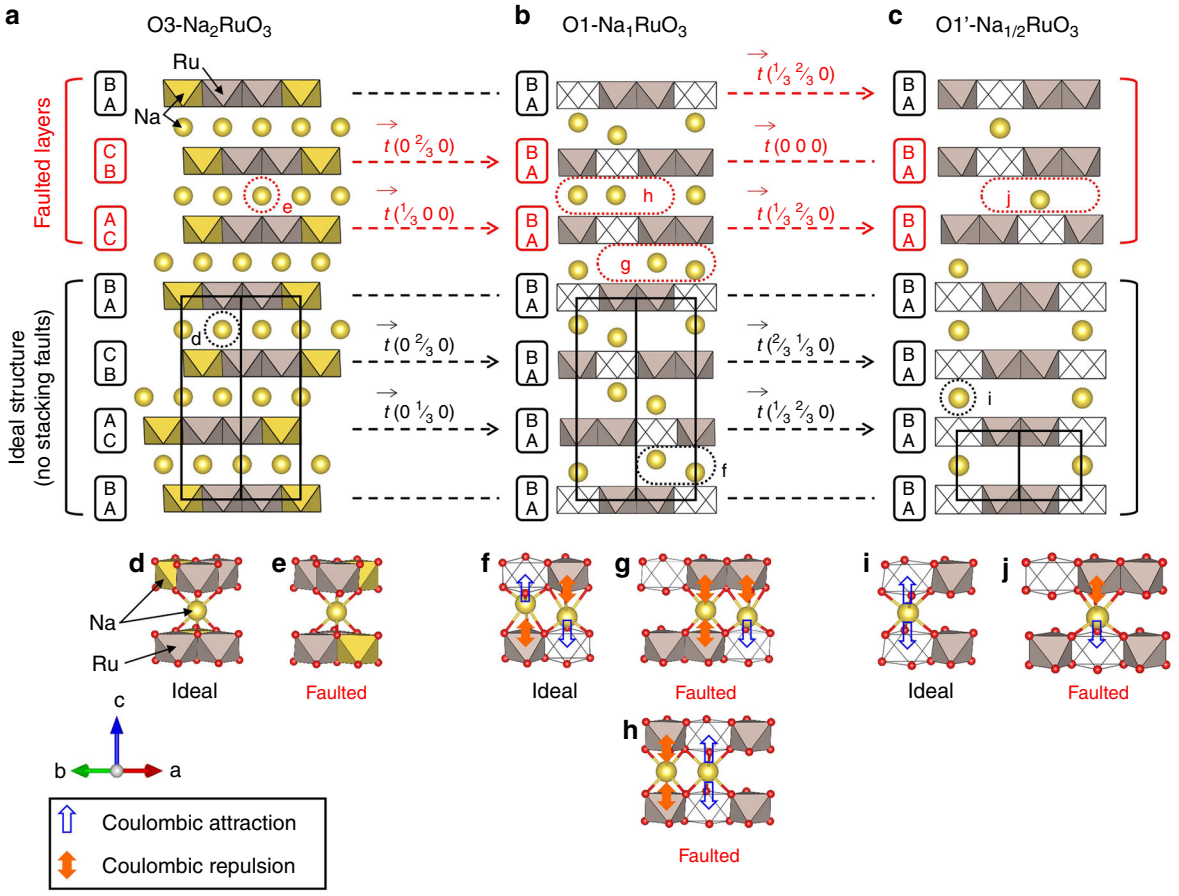

Fig. 4 Coulombic forces and resultant stacking-fault-depression (self-ordering) in $Na_{2-x}RuO_3$. Structural representation and projected stacking sequences of the Ru atoms of **a** O3-Na_2RuO_3, **b** O1-Na_1RuO_3 and **c** O1′-$Na_{1/2}RuO_3$. The monoclinic cell of O3-Na_2RuO_3 has been converted to a pseudo-hexagonal supercell (black lines) for comparison. The transition vectors in the hexagonal supercell from one $[Ru_{2/3}Na_{1/3}]O_2$ or $[Ru_{2/3}\square_{1/3}O_2]$ layer to another are indicated with respect to the pseudo-hexagonal or hexagonal cells. Note that the transition vectors assigned to faulted layers are a few examples out of many possibilities listed in Supplementary Figs. 5 and 6. **d–j** Comparison of the Na environments in ideal and faulted stacking highlighted with dashed circles in the structures shown in **a–c**

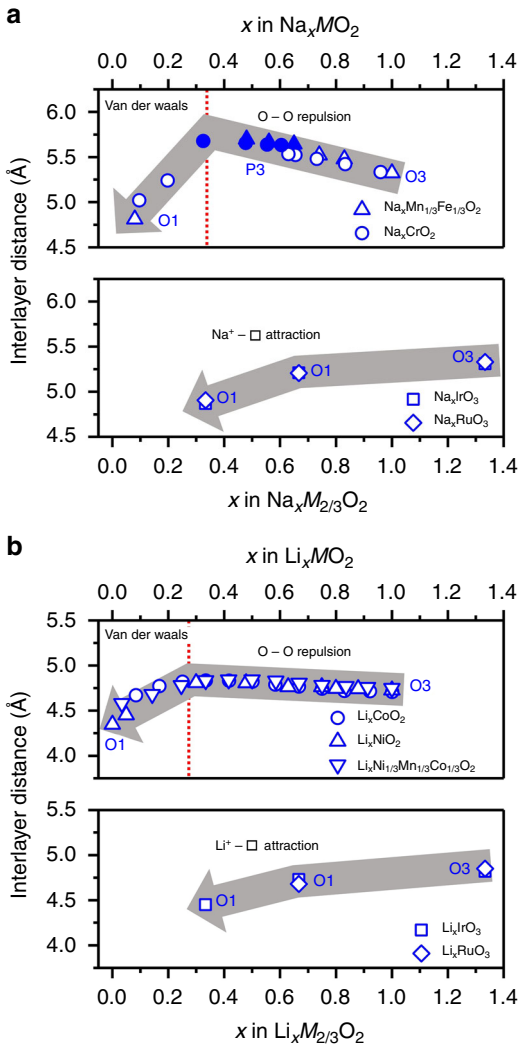

Fig. 5 Overviewing dominant forces for phase transformation during A^+ de-intercalation from AMO_2 and A_2MO_3. Comparison of the general trends in interlayer distance evolution between **a** Na_xMO_2 (M = Cr[28] and $Fe_{2/3}Mn_{1/3}$[8]) and Na_2MO_3 (M = Ru (this study) and Ir[22]) and **b** Li_xMO_2 (M = Co[4], Ni[6] and $Ni_{1/3}Mn_{1/3}Co_{1/3}$[7]) and Li_xMO_3 (M = Ru[17] and Ir[18])

$[Ru_{2/3}Na_{1/3}]O_2$ (or $[Ru_{2/3}\square_{1/3}]O_2$) layers (Fig. 4a–c). Note that the vectors are given in the pseudo-hexagonal cell (O3-Na_2RuO_3) or in the hexagonal cells (O1-Na_1RuO_3 and O1′-$Na_{1/2}RuO_3$; Supplementary Table 7). In O3-Na_2RuO_3 (Fig. 4a), the NaO_6 octahedron in Na layers shares edges with two NaO_6 and four RuO_6 octahedra in the adjacent $[Ru_{2/3}Na_{1/3}]O_2$ layers (Fig. 4d). As the stacking faults only impact the stacking of the $[Ru_{2/3}Na_{1/3}]O_2$ layers, the Na^+ ions in the Na layer have the same local environment (Fig. 4e) and it can be considered that a different stacking is equally probable in O3-Na_2RuO_3. However, in O1-Na_1RuO_3 consisting of honeycomb ordered $[Ru_{2/3}\square_{1/3}]O_2$ and $[Na_{2/3}\square_{1/3}]O_2$ layers with the ABAB oxygen packing (Fig. 4b), all the octahedral positions in the slab share faces with the octahedral positions of the interslab space (Supplementary Fig. 6). As a result, the gliding vectors $\vec{t}$ that shift each layer of O3-Na_2RuO_3 to the ones of O1-Na_1RuO_3 are ideally adjusted to set each NaO_6 octahedron in the $[Na_{2/3}\square_{1/3}]$ layers to share faces with a $\square O_6$ octahedron and a RuO_6 octahedron in the adjacent $[Ru_{2/3}\square_{1/3}]O_2$ layers (Fig. 4f and Supplementary Fig. 7). The stronger attraction of the oxygen atoms surrounding a vacancy on the Na^+ ion (later referred to as $Na^+-\square$ Coulombic attraction for simplicity) and the Na^+-Ru^{5+} Coulombic repulsion cooperatively displace the Na^+ ion toward $\square$[20]. When assuming the hypothetical stacking faults (Fig. 4g, h), one of two NaO_6 octahedra is trapped between two RuO_6 octahedra, where strong $Ru^{5+}-Na^+-Ru^{5+}$ Coulombic repulsions make the faulted structural option unfavorable. Consequently, during the O3 to O1 transformation, slab gliding tends to occur in a way which minimizes the Coulombic energy and as a consequence removes the stacking faults, as described in Fig. 4 and Supplementary Fig. 7. Owing to the three-directional gliding possibilities, most of the stacking faults disappear during the transformation. However, the NaO_6 octahedron can occasionally be stabilized by the local $\square-Na^+-\square$ Coulombic attraction (Fig. 4h), and some stacking faults may remain in O1-Na_1RuO_3.

On the other hand, in O1′-$Na_{1/2}RuO_3$ (Fig. 4c and Supplementary Fig. 3b), which consists of honeycomb ordered alternating $[Ru_{2/3}\square_{1/3}]O_2$ and $[Na_{1/3}\square_{2/3}]$ layers, the NaO_6 octahedron shares faces with two $\square O_6$ octahedra in the adjacent $[Ru_{2/3}\square_{1/3}]O_2$ layers (Fig. 4c, i). Again with hypothetical stacking faults resulting from $\vec{t}$ different from the ideal ones shown in Supplementary Fig. 8, the NaO_6 octahedron in the $[Na_{1/3}\square_{2/3}]$ layer shares faces with $\square O_6$ and RuO_6 octahedra, and the local Na^+-Ru^{5+} Coulombic repulsion prohibits the formation of the faulted structure (Fig. 4j). Therefore, the amount of the stacking faults in Na_xRuO_3 ($1/2 \le x \le 2$) continuously diminishes as desodiation proceeds, because the ordered stacking sequences become electrostatically more favorable. As discussed above, no peculiar local environment is stabilized in O3-Na_2RuO_3, which allows for stacking faults reformation upon sodiation (Supplementary Figs. 4 and 5).

Discussion

The aforementioned importance of the attractive $A^+-\square$ and repulsive A^+-M^{5+} Coulombic interactions can lead to more general discussions on the phase stability of A_2MO_3 and AMO_2 upon charging. Figure 5a shows the experimental evolution of the interlayer distance upon charging various Na_xMO_2 (M = 3d)[8,28] and Na_2MO_3 (M = 4d, 5d)[22] compounds as a function of the sodium content. Figure 5b shows the similar plots for the lithium analogs, $LiMO_2$ and Li_2MO_3[4,6,7,17,18]. It is noteworthy that all AMO_2 (A = Li, Na and M = 3d) and all A_2MO_3 (A = Li, Na and M = 4d, 5d) respectively follow the same tendencies.

As mentioned in the introduction, the phase transformation of A_xMO_2 is dominated by the competing O−O Coulombic repulsion ($0.4 < x < 1.0$) and van der Waals attraction ($0 < x < 0.4$) between adjacent MO_2 layers[4–8], which initiates the increase of the interlayer distance ($0.4 < x < 1.0$) followed by its abrupt decrease upon deeper charging ($0 < x < 0.4$). Structural evolution in the "Coulombic domain" with large A^+ content ($0.4 < x < 1.0$) are highly reversible and is the basis of commercial positive electrode materials such as $LiCoO_2$ and $Li[Ni_{1-y-z}Mn_yCo_z]O_2$, while the "van der Waals domain" with smaller A^+ content ($0 < x < 0.4$) marks the limit of reversibility of many practical layered oxides as a result of cation migration, spinel transformation, crack formation, and delamination/exfoliation[8–13].

On the contrary, the highly ordered nature of the $[Ru_{2/3}\square_{1/3}]O_2$ layers of A_xMO_3 (M = Ru or Ir) triggers a progressive gain in $A^+-\square$ Coulombic energy upon A^+ extraction as the remaining A^+ ions cooperatively act as robust pillars between adjacent $[Ru_{2/3}\square_{1/3}]O_2$ layers to prevent structural collapse. The slight decrease of the interlayer distance is driven by Coulombic $A^+-\square$ attractive forces which are strong enough to induce the slab glidings, O3 → O1 → O1′, forming a more-ordered structure upon charging. It is this situation that realizes reversible

charge–discharge reactions in ordered A_2MO_3 over a wide compositional domain of the guest ion A^+.

In summary, we identified a spontaneous reorganization of the stacking faults in Na_xRuO_3, a model material to understand oxygen-redox reactions in layered oxides for large-capacity battery electrodes. In particular, the progressive ordering upon charging process is a general phenomenon to A_2MO_3 (A = Li, Na and M = 4d, 5d) materials and is induced by the cooperative effect of maximizing the A^+–□ Coulombic attraction and minimizing the A^+–M^{5+} Coulombic repulsion, which significantly enlarges the reversible operation range of layered oxides. Complementarily to our previous work, in addition to generate redox-active "orphaned" nonbonding oxygen 2*p* orbitals to "activate" additional oxygen-redox reactions, honeycomb ordering of M and □ contribute to "stabilizing" reversible phase transformation. In this regard, the importance of the overall material design that includes ordered vacancies with its neutral charge to attract alkali cations was highlighted. By establishing proper ways to control the stacking faults[29–31] or vacancies[32], the concept of progressive ordering upon charging may be extended to stabilize other related compounds[33].

Methods

Synthesis of Na_2RuO_3. Na_2RuO_3 was prepared according to the literature[25]. First, Na_2RuO_4 is prepared by mixing stoichiometric amounts of Na_2O_2 (Sigma-Aldrich) and RuO_2 (Kanto chemicals). Pellets are then made and introduced in a tubular furnace to be annealed at 650 °C for 12 h under O_2 atmosphere. After the synthesis, Na_2RuO_4 is grinded and shaped into pellets again to be thermally decomposed into Na_2RuO_3 at 850 °C for 12 h under Ar atmosphere. After cooling down to room temperature, the sample is introduced in an Ar filled glovebox.

Characterization. The synchrotron XRD patterns were recorded at Aichi Synchrotron Radiation Center (Aichi-SR, O3-Na_2RuO_3), and Photon Factory at High Energy Accelerator Research organization (KEK-PF, BL-8B) or SPring-8 (O1-Na_1RuO_3 and O1′-$Na_{1/2}RuO_3$, beamline 02B2). All samples were protected from air exposure during the measurement. Rietveld refinement was performed using Jana2006[34]. Analyses of the stacking faults in the materials were carried out using the FAULTS software[27]. The crystal structures were drawn using VESTA[35]. Selected Area Electron Diffraction (SAED) patterns were recorded using an electron microscope (HF-3000S; Hitachi Ltd. and Titan Cubed; FEI Co.) operated at 300 kV. The camera length for SAED was calibrated with a Si crystal.

Electrochemistry. Electrochemical measurements were carried out in Na_2RuO_3/electrolyte/Na half-cells assembled in CR2032 type coin cells. The electrolyte was 1 mol/L $NaPF_6$ in EC:DEC (1:1) purchased from Chameleon Reagent. Positive electrodes were prepared by coating a slurry made of active material (80 wt%) mixed with acetylene black (10 wt%) and polyvinylidene (10 wt%) in NMP onto Al foil. Sixteen-mm-diameter electrodes were cut after drying for one night under vacuum at 120 °C. The positive and negative electrodes were separated by a layer of Whatman glass fiber separator soaked with electrolyte. The galvanostatic curve was recorded and controlled using a TOSCAT-3100 battery tester. The charge/discharge rate was C/10 which corresponds to the (de)intercalation of 1 Na^+ per Na_xRuO_3 in 10 hours. The O1-Na_1RuO_3 and O1′-$Na_{1/2}RuO_3$ samples were prepared by cycling sintered pellets (diameter 10 mm, weight ≈10–15 mg) of O3-Na_2RuO_3 at C/50 (one Na^+ exchanged in 50 h) until a given voltage (3.07 V and 4.0 V vs. Na/Na^+ for O1-Na_1RuO_3 and O1′-$Na_{1/2}RuO_3$, respectively). The recovered materials were then washed 3 to 5 times with dimethyl carbonate in the glovebox before sending to the synchrotron facility.

In situ X-ray diffraction. In situ XRD was carried out in operando using an in situ cell purchased from Bruker on a Bruker-AXS D8 ADVANCE (Co *K*α radiation) in 0.02° steps over the 2*θ* range of 17–25° at a C/10 rate. The cell configuration is similar to the one described above except for the positive electrode that consisted in a mixture of Na_2RuO_3 (85 wt%), acetylene black (10 wt%), and polytetrafluoroethylene (5 wt%). Two layers of glass fiber separators were used to prevent dendrite formation.

Data availability

The whole datasets are available from the corresponding author on request.

Received: 21 February 2019 Accepted: 12 March 2019
Published online: 16 May 2019

References

1. Mizushima, K., Jones, P. C., Wiseman, P. J. & Goodenough, J. B. Li_xCoO_2 (0 < x < 1): a new cathode material for batteries of high energy density. *Mater. Res. Bull.* **15**, 783–789 (1980).
2. Delmas, C., Braconnier, J.-J., Fouassier, C. & Hagenmuller, P. Electrochemical intercalation of sodium in Na_xCoO_2 bronzes. *Solid State Ion.* **3–4**, 165–169 (1981).
3. Yoshino, A. The birth of the lithium-ion battery. *Angew. Chem. Int. Ed.* **51**, 5798–5800 (2012).
4. Laubach, S. et al. Changes in the crystal and electronic structure of $LiCoO_2$ and $LiNiO_2$ upon Li intercalation and deintercalation. *Phys. Chem. Chem. Phys.* **11**, 3278–3289 (2009).
5. Li, W., Reimers, J. N. & Dahn, J. R. In situ X-ray diffraction and electrochemical studies of $Li_{1-x}NiO_2$. *Solid State Ion.* **67**, 123–130 (1993).
6. Pouillerie, C., Croguennec, L. & Delmas, C. The $Li_xNi_{1-y}Mg_yO_2$ ($y = 0.05$, 0.10) system: structural modifications observed upon cycling. *Solid State Ion.* **132**, 15–29 (2000).
7. Yabuuchi, N., Makimura, Y. & Ohzuku, T. Solid-state chemistry and electrochemistry of $LiCo_{1/3}Ni_{1/3}Mn_{1/3}O_2$ for advanced lithium-ion batteries III. Rechargeable capacity and cycleability. *J. Electrochem. Soc.* **154**, A314–A321 (2007).
8. Mortemard de Boisse, B. et al. O3-$Na_xMn_{1/3}Fe_{2/3}O_2$ as a positive electrode material for Na-ion batteries: structural evolutions and redox mechanisms upon Na^+ (de)intercalation. *J. Mater. Chem. A* **3**, 10976–10989 (2015).
9. Chen-Wiegart, Y.-cK., Liu, Z., Faber, K. T., Barnett, S. A. & Wang, J. 3D analysis of a $LiCoO_2$-$Li(Ni_{1/3}Mn_{1/3}Co_{1/3})O_2$ Li-ion battery positive electrode using x-ray nano-tomography. *Electrochem. Commun.* **28**, 127–130 (2013).
10. Basch, A., de Campo, L., Albering, J. H. & White, J. W. Chemical delithiation and exfoliation of Li_xCoO_2. *J. Solid State Chem.* **220**, 102–110 (2014).
11. Rougier, A., Gravereau, P. & Delmas, C. Optimization of the composition of the $Li_{1-z}Ni_{1+z}O_2$ electrode materials: structural, magnetic, and electrochemical studies. *J. Electrochem. Soc.* **143**, 1168–1175 (1996).
12. Kim, S., Ma, X., Ong, S. P. & Ceder, G. A comparison of destabilization mechanisms of the layered Na_xMO_2 and Li_xMO_2 compounds upon alkali de-intercalation. *Phys. Chem. Chem. Phys.* **14**, 15571–15578 (2012).
13. Choi, S. & Manthiram, A. Factors influencing the layered to spinel-like phase transition in layered oxide cathodes. *J. Electrochem. Soc.* **149**, A1157–A1163 (2002).
14. Lu, Z., Beaulieu, L. Y., Donaberger, R. A., Thomas, C. L. & Dahn, J. R. Synthesis, structure, and electrochemical behavior of $Li[Ni_xLi_{1/3-2x/3}Mn_{2/3-x/3}]O_2$. *J. Electrochem. Soc.* **149**, A778–A791 (2002).
15. Koga, H. et al. Reversible oxygen participation to the redox processes revealed for $Li_{1.20}Mn_{0.54}Co_{0.13}Ni_{0.13}O_2$. *J. Electrochem. Soc.* **160**, A786–A792 (2013).
16. Koga, H. et al. Different oxygen redox participation for bulk and surface: a possible global explanation for the cycling mechanism of $Li_{1.20}Mn_{0.54}Co_{0.13}Ni_{0.13}O_2$. *J. Power Sources* **236**, 250–258 (2013).
17. Sathiya, M. et al. Reversible anionic redox chemistry in high-capacity layered-oxide electrodes. *Nat. Mater.* **12**, 827–835 (2013).
18. McCalla, E. et al. Visualization of O-O peroxo-like dimers in high-capacity layered oxides for Li-ion batteries. *Science* **350**, 1516–1521 (2015).
19. Sathiya, M. et al. High performance $Li_2Ru_{1-y}Mn_yO_3$ ($0.2 < y < 0.8$) cathode materials for rechargeable lithium-ion batteries: their understanding. *Chem. Mater.* **25**, 1121–1131 (2013).
20. Mortemard de Boisse, B. et al. Intermediate honeycomb ordering to trigger oxygen redox chemistry in layered battery electrode. *Nat. Commun.* **7**, 11397 (2016).
21. Rozier, P. et al. Anionic redox chemistry in Na-rich $Na_2Ru_{1-y}Sn_yO_3$ positive electrode material for Na-ion batteries. *Electrochem. Commun.* **53**, 29–32 (2015).
22. Perez, A. J. et al. Strong oxygen participation in the redox governing the structural and electrochemical properties of Na-rich layered oxide Na_2IrO_3. *Chem. Mater.* **28**, 8278–8288 (2016).
23. Luo, K. et al. Charge-compensation in 3*d*-transition-metal-oxide intercalation cathodes through the generation of localized electron holes on oxygen. *Nat. Chem.* **8**, 684–691 (2016).
24. Sathiya, M. et al. Origin of voltage decay in high-capacity layered oxide electrodes. *Nat. Mater.* **14**, 230–238 (2015).
25. Mogare, K. M., Friese, K., Klein, W. & Jansen, M. Syntheses and crystal structures of two sodium ruthenates: Na_2RuO_4 and Na_2RuO_3. *Z. Anorg. Allg. Chem.* **630**, 547–552 (2004).
26. Delmas, C., Fouassier, C. & Hagenmuller, P. Structural classification and properties of the layered oxides. *Physica* **99**, 81–85 (1980).
27. Casas-Cabanas, M., Reynaud, M., Rikarte, J., Horbach, P. & Rodriguez-Carvajal, J. FAULTS: a program for refinement of structures with extended defects. *J. Appl. Cryst.* **49**, 2259–2269 (2016).

28. Kubota, K. et al. New insight into structural evolution in layered $NaCrO_2$ during electrochemical sodium extraction. *J. Phys. Chem. C* **119**, 166–175 (2015).
29. Boulineau, A., Croguennec, L., Delmas, C. & Weill, F. Structure of Li_2MnO_3 with different degrees of defects. *Solid State Ion.* **180**, 1652–1659 (2010).
30. Kobayashi, H., Tabuchi, M., Shikano, M., Kageyama, H. & Kanno, R. Structure, and magnetic and electrochemical properties of layered oxides, Li_2IrO_3. *J. Mater. Chem.* **13**, 957–962 (2003).
31. Serrano-Sevillano, J. et al. Enhanced electrochemical performance of Li-rich cathode materials through microstructural control. *Phys. Chem. Chem. Phys.* **20**, 23112–23122 (2018).
32. Mortemard de Boisse, B. et al. Highly reversible oxygen-redox chemistry at 4.1 V in $Na_{4/7-x}[\square_{1/7}Mn_{6/7}]O_2$ ($\square$: Mn vacancy). *Adv. Energy Mater.* **8**, 180409 (2018).
33. Assadi, M. H. N., Okubo, M., Yamada, A. & Tateyama, Y. Oxygen redox in hexagonal layered Na_xTMO_3 (TM=4d elements) for high capacity Na ion batteries. *J. Mater. Chem. A* **6**, 3747–3753 (2018).
34. Petricek, V., Dusek, M. & Palatinus, L. Crystallographic computing system JANA2006: general features. *Z. Krist.* **229**, 345–352 (2014).
35. Momma, K. & Izumi, F. *VESTA 3* for three-dimensional visualization of crystal, volumetric and morphology data. *J. Appl. Cryst.* **44**, 1272–1276 (2011).

Acknowledgements

This work was supported by a JSPS Grant-in-Aid for Specially Promoted Research (No. 15H05701). This work was also financially supported by the Ministry of Education, Culture, Sports, Science and Technology (MEXT), Japan under the "Elemental Strategy Initiative for Catalysts and Batteries (ESICB)". M.O. was supported by JSPS KAKENHI Grant Number JP18K19124. The synchrotron powder diffraction experiment for structure analyses were performed at BL5S2 of Aichi-SR (Proposal No. 2017D3004, 2017D3010, and 2017D4010), BL-8B of KEK-PF (Proposal No. 2015G684) and BL02B2 of SPring-8 (2015A1503). B.M.B. acknowledges the Japan Society for the Promotion of Science for his JSPS fellowship. M.R. acknowledges the support of the Spanish Ministerio de Economía y Competitividad (MINECO) through her research fellowship (reference number FJCI-2014–19990). M.R. and M.C.C. thank MINECO for financial support (reference numbers: ENE2016–81020-R and ENE2016–75242-R).

Author contributions

B.M.B., M.O., and A.Y. conceived and directed the project. B.M.B. and J.M. synthesized Na_2RuO_3. B.M.B. characterized Na_2RuO_3. J.K. measured SAED patterns. S.N. conducted synchrotron X-ray diffraction experiments. B.M.B., M.R., and M.C.C. conducted FAULT analysis. B.M.B. and C.D. analyzed the phase transformations. All authors wrote the manuscript.

Additional information

Supplementary Information accompanies this paper at https://doi.org/10.1038/s41467-019-09409-1.

Competing interests: The authors declare no competing interests.

Reprints and permission information is available online at http://npg.nature.com/reprintsandpermissions/

Journal peer review information: *Nature Communications* thanks the anonymous reviewer(s) for their contribution to the peer review of this work.

Publisher's note: Springer Nature remains neutral with regard to jurisdictional claims in published maps and institutional affiliations.

Open Access This article is licensed under a Creative Commons Attribution 4.0 International License, which permits use, sharing, adaptation, distribution and reproduction in any medium or format, as long as you give appropriate credit to the original author(s) and the source, provide a link to the Creative Commons license, and indicate if changes were made. The images or other third party material in this article are included in the article's Creative Commons license, unless indicated otherwise in a credit line to the material. If material is not included in the article's Creative Commons license and your intended use is not permitted by statutory regulation or exceeds the permitted use, you will need to obtain permission directly from the copyright holder. To view a copy of this license, visit http://creativecommons.org/licenses/by/4.0/.

© The Author(s) 2019